# Supplementary Material to *From ice core to ground-penetrating radar: representativeness of SMB at three ice rises along the Princess Ragnhild Coast, East Antarctica*

Marie G.P. CAVITTE[1], Hugues GOOSSE[1], Sarah WAUTHY[2], Thore KAUSCH[3], Jean-Louis TISON[2], Brice VAN LIEFFERINGE[4], Frank PATTYN[2], Jan T.M. LENAERTS[5], Philippe CLAEYS[6]

[1]*Georges Lemaître Centre for Earth and Climate Research (TECLIM), Earth and Life Institute (ELI), Université catholique de Louvain (UCL), Louvain-la-Neuve, Belgium*
[2]*Laboratoire de Glaciologie, Université libre de Bruxelles (ULB), Brussels, Belgium*
[3]*Department of Geoscience & Remote Sensing, Delft University of Technology, Mekelweg 5, 2628 CD Delft, the Netherlands*
[4]*Non-academic*
[5]*Department of Atmospheric and Oceanic Sciences, University of Colorado Boulder, Boulder CO, USA*
[6]*Analytical, Environmental and Geo-Chemistry, Vrije Universiteit Brussel (VUB), Brussels, Belgium*
*Correspondence: Marie Cavitte <marie.cavitte@uclouvain.be>*

## SUPPLEMENT 1: RADAR TRANSECTS AND TRACED IRHS

Figs. S1-S3 show typical radar transects for the three ice rises, with the traced IRHs indicated. The transects chosen for each ice rise are the same as for Fig. 2 of the main manuscript, and Figs. S3 and S5 of this supplement.

## SUPPLEMENT 2: BEST-FIT DEPTH-DENSITIES

Note that because the raw density measurements are noisy (Fig. S4), we use an exponential fit of the depth-density profiles, based on the curve defined at DIR by Hubbard and others (2013), adapted to all three ice core sites to obtain the best r-squared fit. All densities, $\rho$, are given in g cm$^{-3}$ and depths, $z$, are given in meters.

At HIR, the best-fit profile (Fig. S4, panel a) is given by

$$\rho = 0.910 - 0.465 * e^{-0.028z}, \tag{1}$$

with an $R^2$ value of 0.9962.

At DIR, the best-fit profile obtained (Fig. S4, panel b) is given by

$$\rho = 0.910 - 0.510 * e^{-0.026z}, \tag{2}$$

with an $R^2$ value of 0.9824.

And finally, at LIR, the best-fit profile (Fig. S4, panel c) is

$$\rho = 0.910 - 0.450 * e^{-0.030z}, \tag{3}$$

with an $R^2$ value of 0.9960.

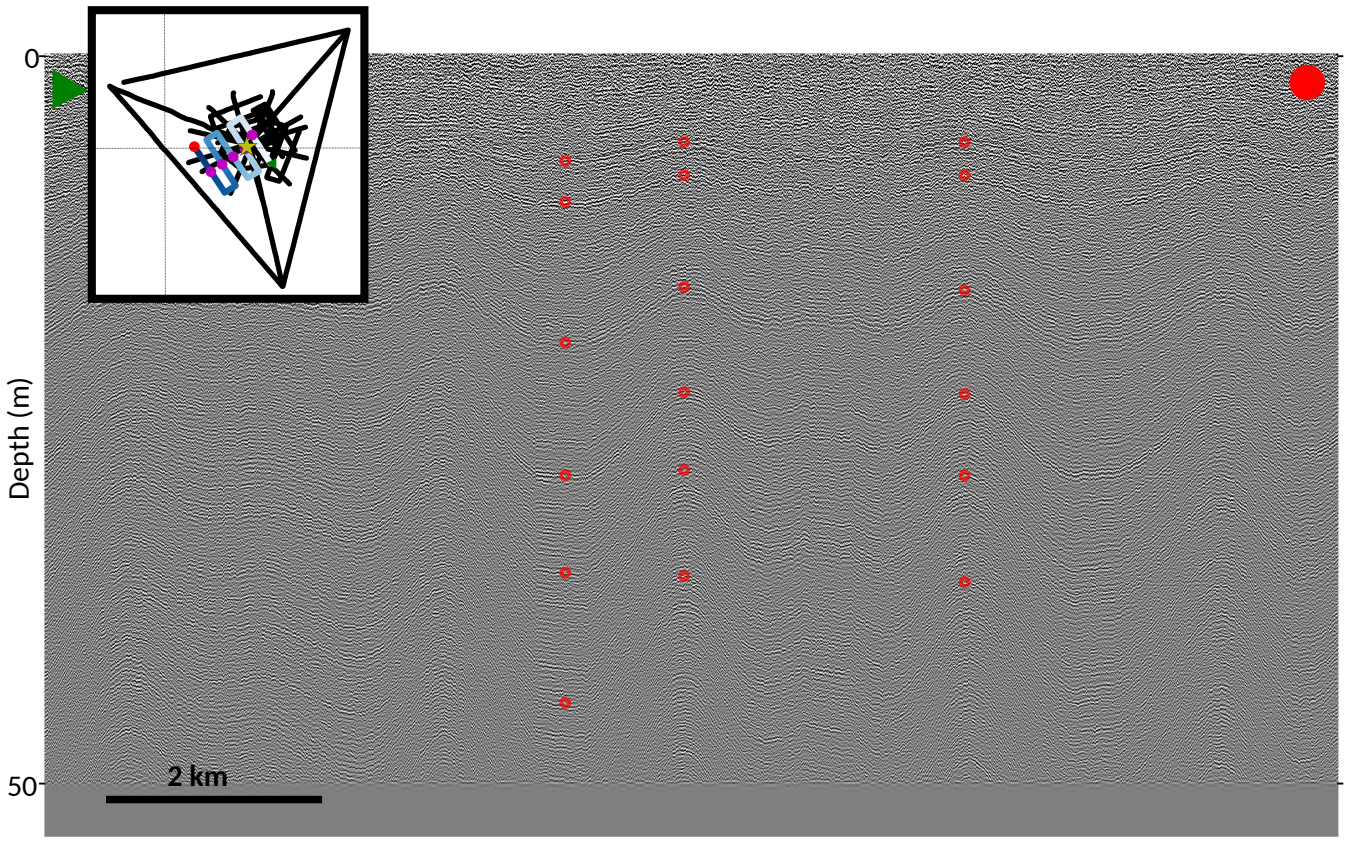


**Fig. S1.** Radar transect crossing the ice divide at HIR (same transect as Fig. 2 of the main manuscript). The six IRHs traced are indicated by red circles. The inset displays the whole radar survey with the radar transect shown in blue; magenta crosses indicate the divide intersections, green and red dots (matching those on the radar transect) indicate the start and end of the radar transect, respectively, a yellow star locates the ice core site.

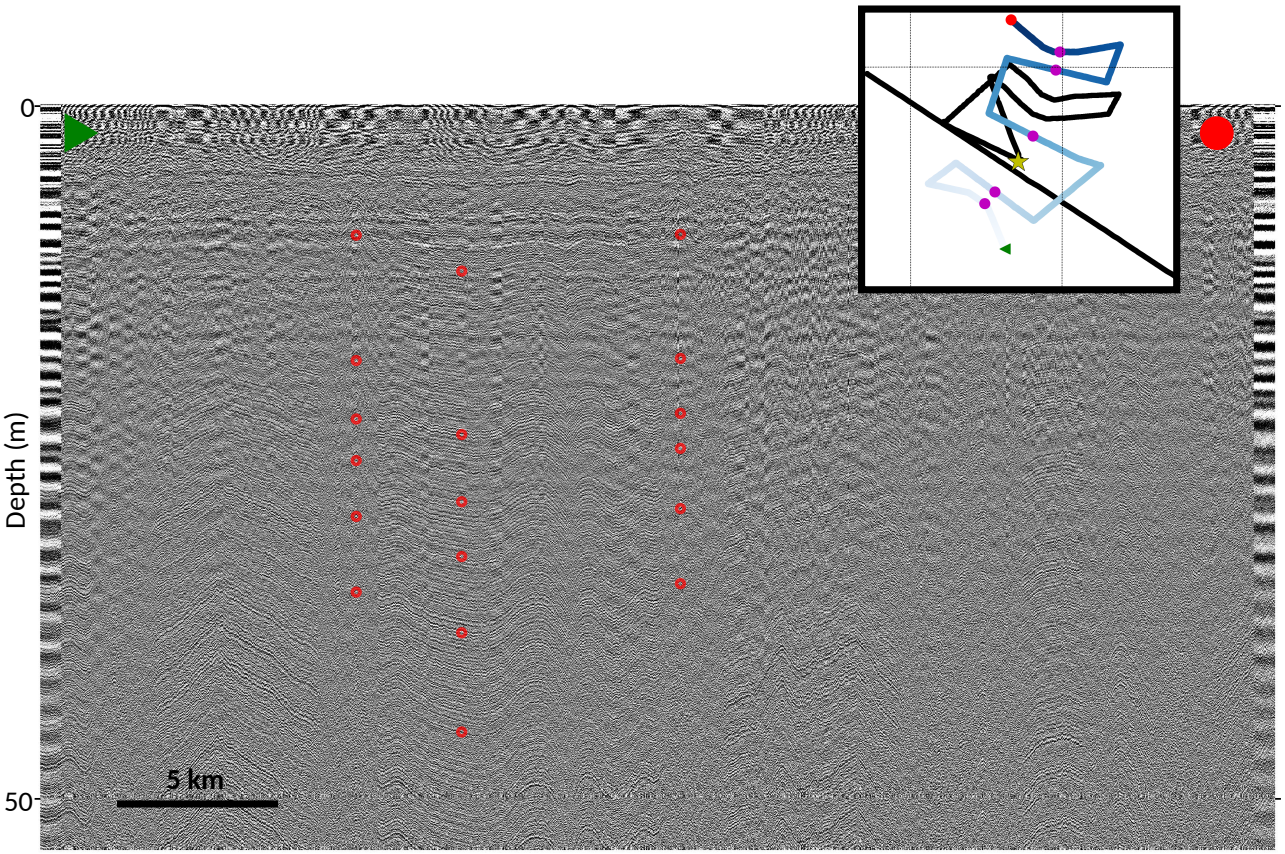


**Fig. S2.** Radar transect crossing the ice divide at DIR (same transect as Fig. S5). The six IRHs traced are indicated by red circles. The inset displays the whole radar survey with the radar transect shown in blue; magenta crosses indicate the divide intersections, green and red dots (matching those on the radar transect) indicate the start and end of the radar transect, respectively, a yellow star locates the ice core site.

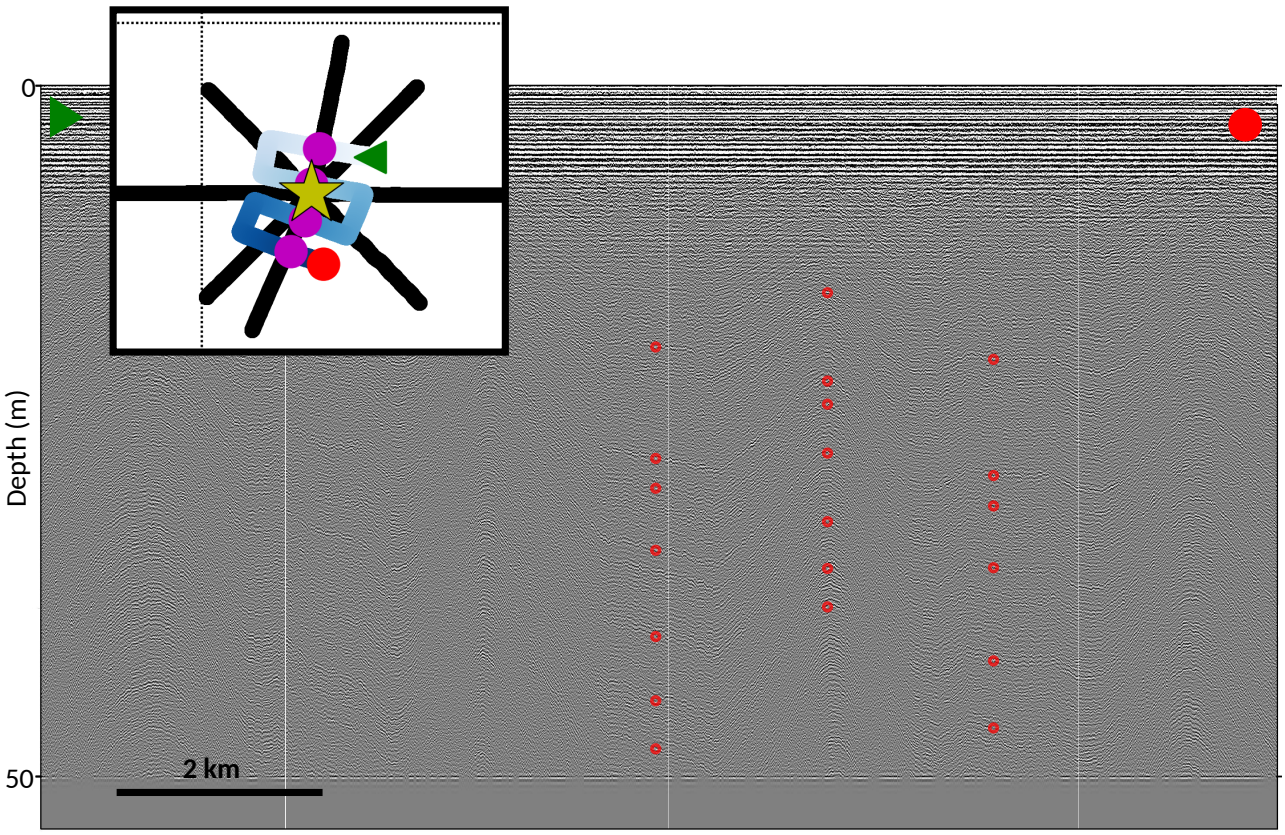


**Fig. S3.** Radar transect crossing the ice divide at LIR (same transect as Fig. S7). The seven IRHs traced are indicated by red circles. The inset displays the whole radar survey with the radar transect shown in blue; magenta crosses indicate the divide intersections, green and red dots (matching those on the radar transect) indicate the start and end of the radar transect, respectively, a yellow star locates the ice core site.

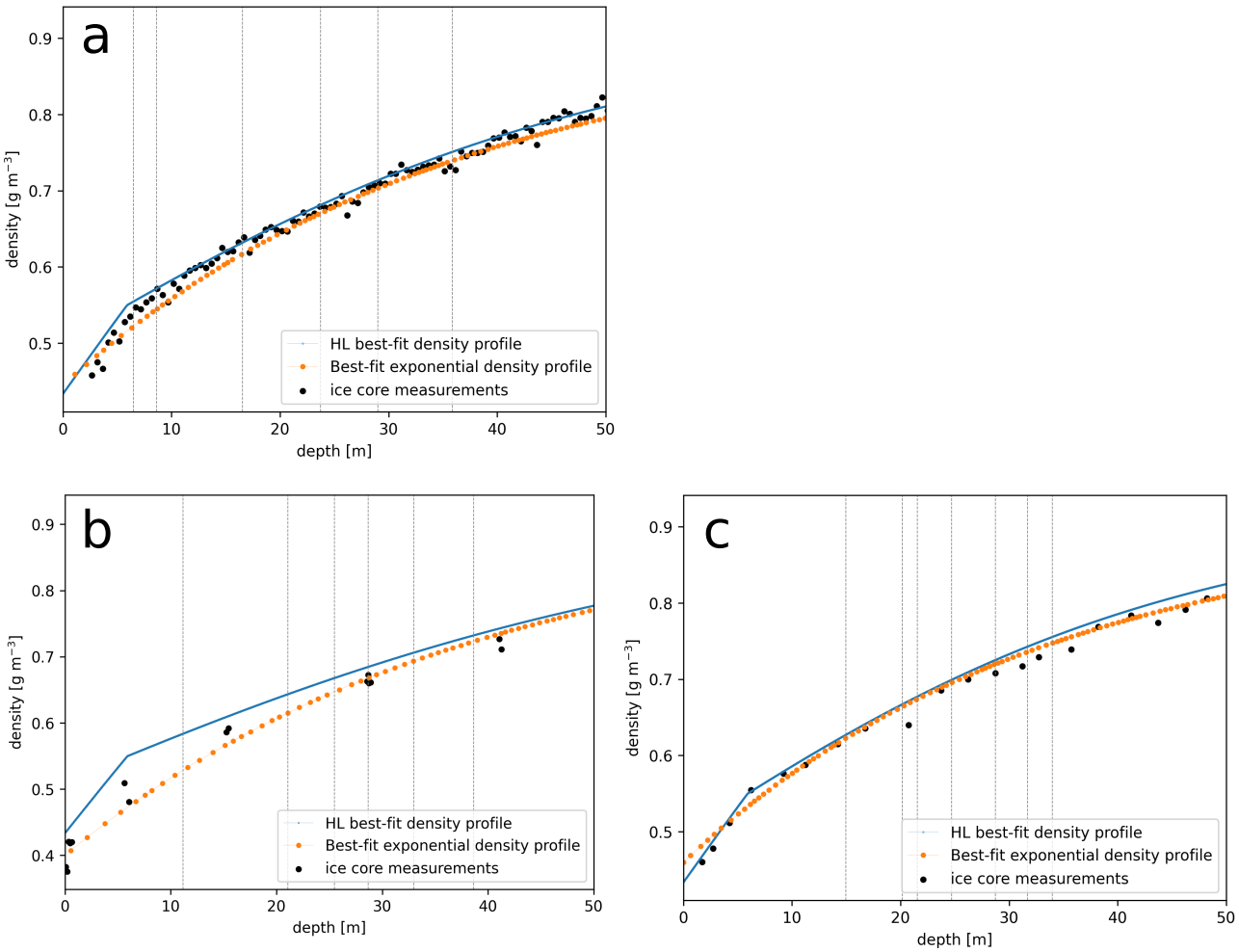


**Fig. S4.** Comparison of measured versus best-fit profiles of depth-density at (a) HIR, (b) DIR and (c) LIR. Black dots show the ice core measured densities, the orange dotted line show the best-fit exponential profiles to the ice core measurements, the blue line shows the best-fit Herron–Langway (HL) firn densification profile (Herron and Langway, 1980) at the closest radar point to the ice core site. Grey vertical lines highlight the IRH depths at the closest point to the ice core site. Note that at DIR, the closest point to the ice core site is the average value over the three most representative sites (see main manuscript).

The HL best-fit profile is obtained after ∼3 iterations, once the pairwise SMB values between two iterations are within 0.005 m w.e. yr$^{-1}$ of each other. We use an initial density of 0.47 g m$^{-3}$, surface accumulation rate of 0.5 m w.e. yr$^{-1}$ and surface air temperature of 257 K, as well as an ice density of 0.917 g cm−3 and calculate the HL density-depth profile at a vertical resolution of 1 cm. The best-fit HL profile obtained at the closest point to the ice core site are shown on Fig. S4.

## SUPPLEMENT 3: SPATIAL DISTRIBUTION OF IRH DEPTHS AND SMB AT DIR AND LIR

Figs. S5-S8 show the spatial distribution of IRH depth and SMB at DIR and LIR, respectively.

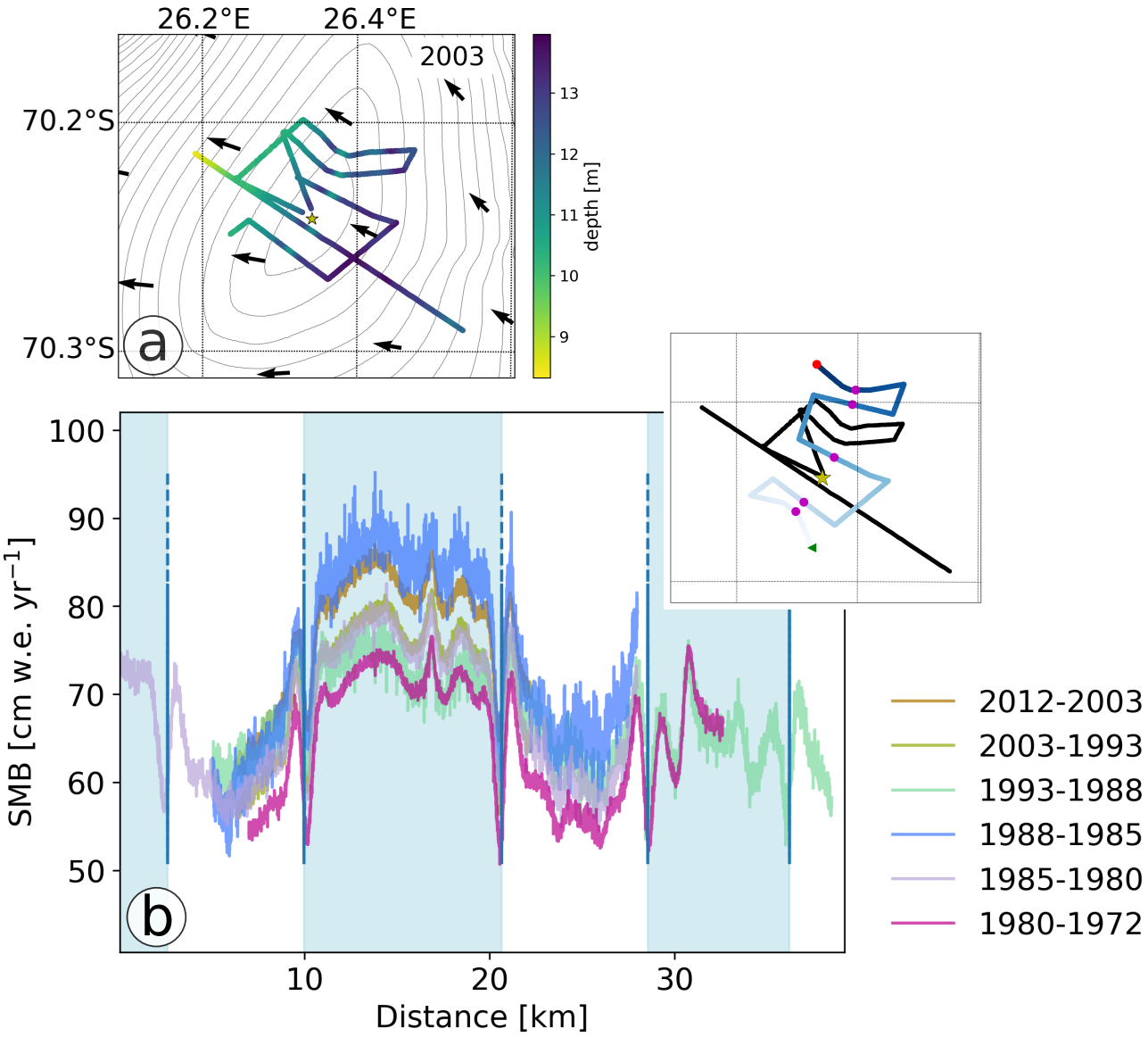


**Fig. S5.** IRH depth and SMB obtained at DIR. (a) Depth of the shallowest IRH. A star locates the ice core site and the mean wind direction is shown by black arrows (RACMO2.3 5.5 km simulations over 1979-2017, Van Wessem and others (2018)). Contours shown are REMA elevations at 20 m intervals (Howat and others, 2019). (b) SMB obtained along the radar transect shown in the inset. Each colored line indicates a different IRH. The windward sides of the ice rise are highlighted in light blue and the ice divide intersections are marked by blue vertical lines. The inset displays the whole radar survey at DIR with the radar transect shown in blue with magenta crosses indicating the divide intersections, green and red dots indicating the start and end of the radar transect, respectively, a yellow star locating the ice core site.

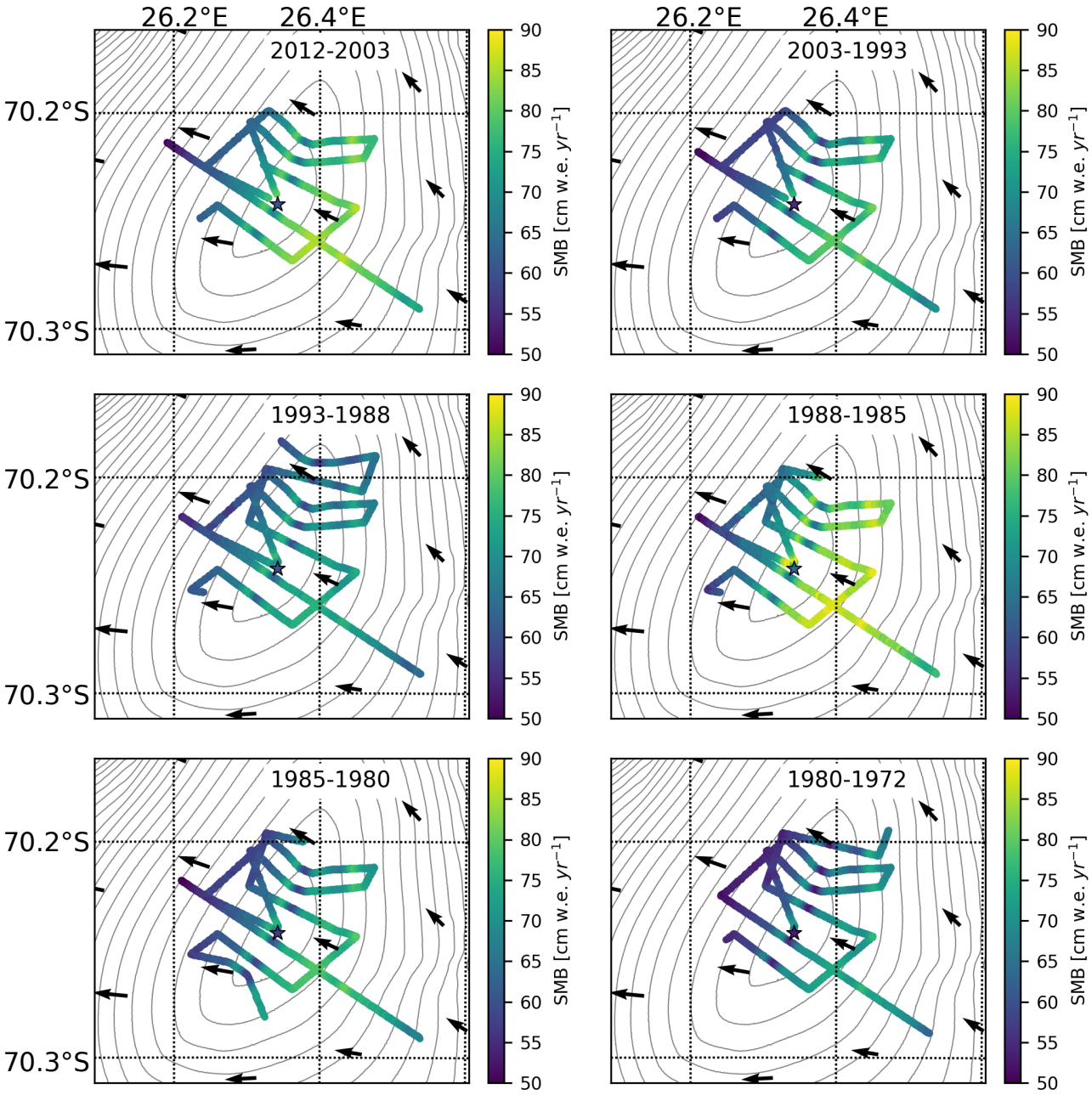


**Fig. S6.** SMB (cm w.e. $yr^{-1}$) calculated per time interval at DIR (indicated on each inset) for the gridded data set (50 × 50 m). The corresponding ice core SMB value is shown by a star on the same color scale as for the radar transects. Contours shown are REMA elevations at 20 m intervals (Howat and others, 2019). Mean wind direction is shown by black arrows (RACMO2.3 5.5 km simulations over 1979-2017, Van Wessem and others (2018))

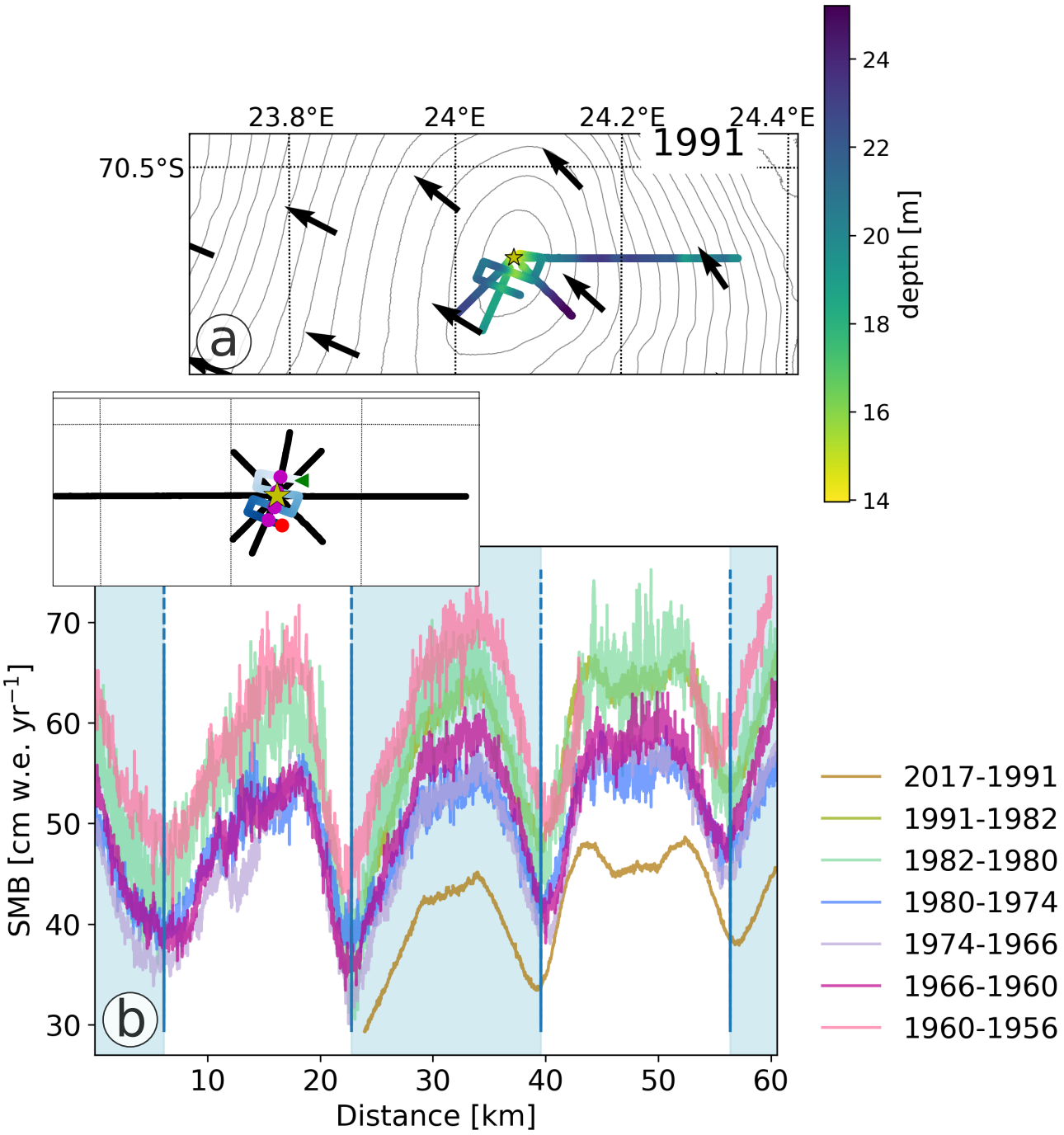


**Fig. S7.** IRH depth and SMB obtained at LIR. (a) Depth of the shallowest IRH. A star locates the ice core site and the mean wind direction is shown by black arrows (RACMO2.3 5.5 km simulations over 1979-2017, Van Wessem and others (2018)). Contours shown are REMA elevations at 20 m intervals (Howat and others, 2019). (b) SMB obtained along the radar transect shown in the inset. Each colored line indicates a different IRH. The windward sides of the ice rise are highlighted in light blue and the ice divide intersections are marked by blue vertical lines. The inset displays the whole radar survey at LIR with the radar transect shown in blue with magenta crosses indicating the divide intersections, green and red dots indicating the start and end of the radar transect, respectively, a yellow star locating the ice core site.

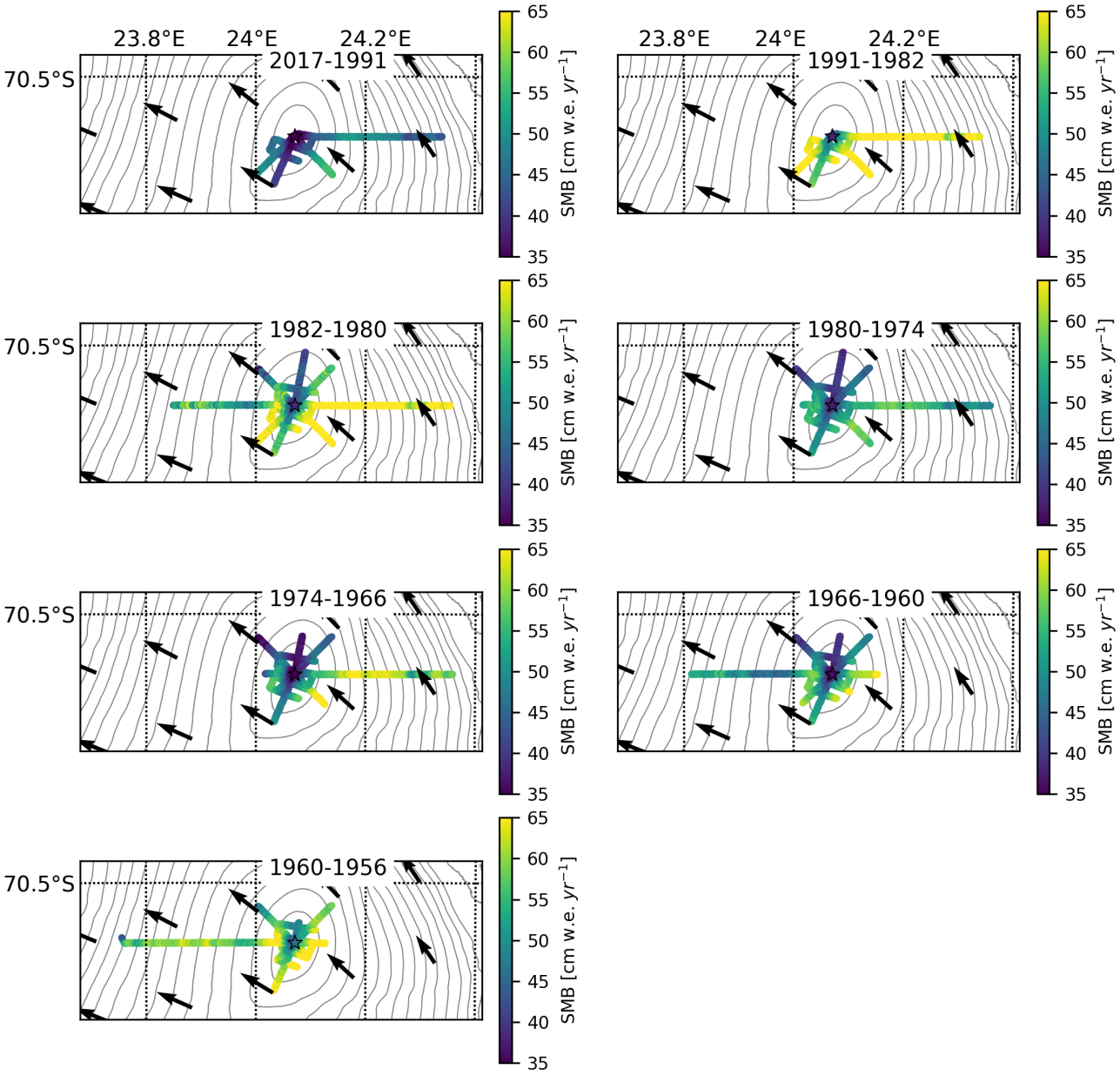


**Fig. S8.** SMB (cm w.e. $yr^{-1}$) calculated per time interval at LIR (indicated on each inset) for the gridded data set (50 × 50 m). The corresponding ice core SMB value is shown by a star on the same color scale as for the radar transects. Contours shown are REMA elevations at 20 m intervals (Howat and others, 2019). Mean wind direction is shown by black arrows (RACMO2.3 5.5 km simulations over 1979-2017, Van Wessem and others (2018))

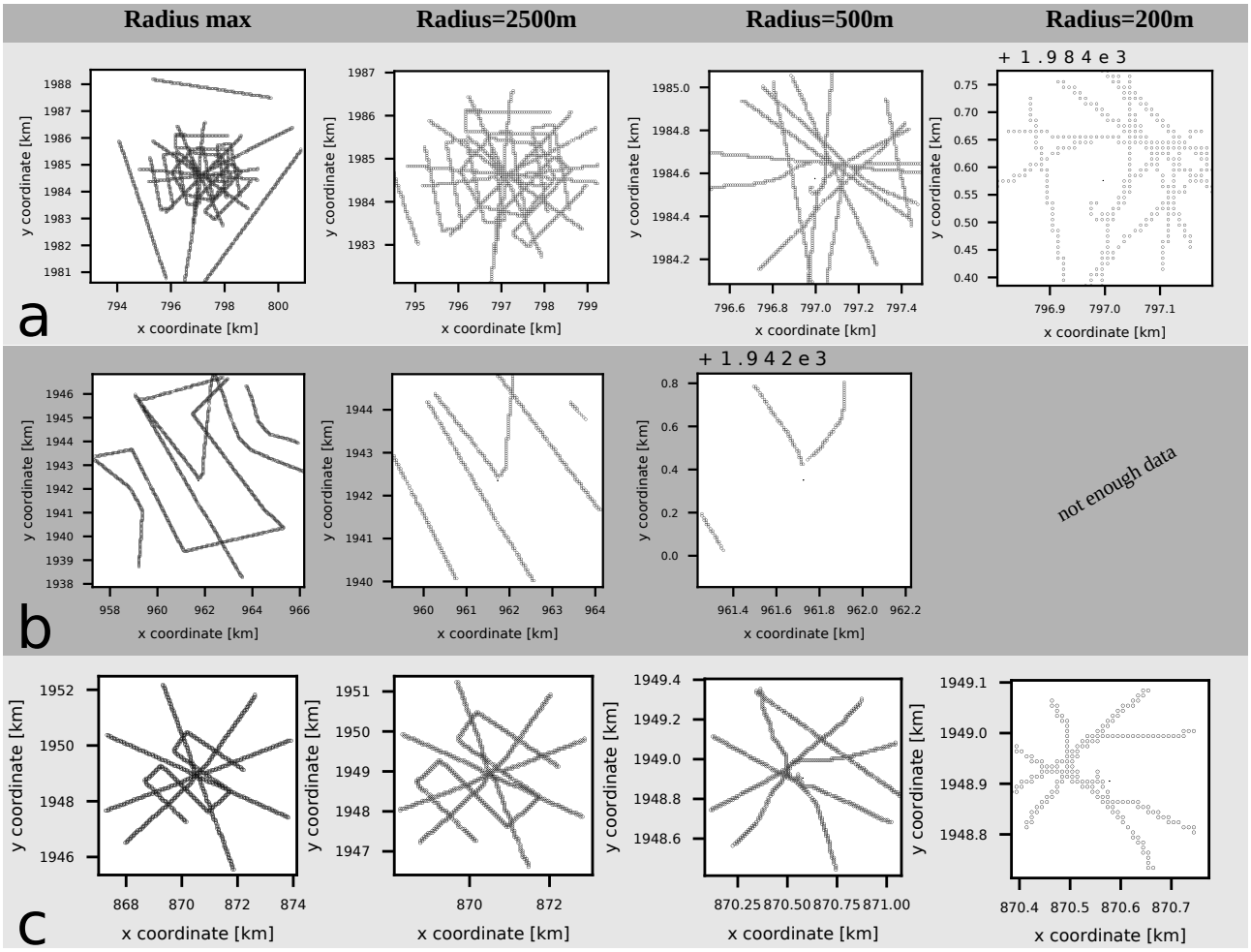


**Fig. S9.** Gridded radar data density (black dotted lines) as a function of radial distance from each ice core site, for (a) HIR, (b) DIR and (c) LIR.

## SUPPLEMENT 4: RADAR DATA DENSITY AS FUNCTION OF RADIUS AWAY FROM THE ICE CORE SITE

Gridded radar data density as a function of the four radial distances from each ice core site, for each ice rise (Fig. S9).

## SUPPLEMENT 5: REPRESENTATIVENESS OF ICE CORE'S SMB MEAN STATE AND TEMPORAL VARIABILITY AS A FUNCTION OF SURFACE AREA, AT DIR AND LIR

Figs. S10 and S11 show the difference in mean and temporal variability of SMB between the ice core and the radar SMB records at DIR and LIR, respectively.

## SUPPLEMENT 6: SPATIAL DISTRIBUTION OF THE SMB ANOMALIES FOR DIR AND LIR

Figs. S12 and S13 show the spatial distribution of the SMB anomalies over each ice rise, for each radar IRH pairs time interval at DIR and LIR, respectively. We use the 50 × 50 m gridded radar product at the

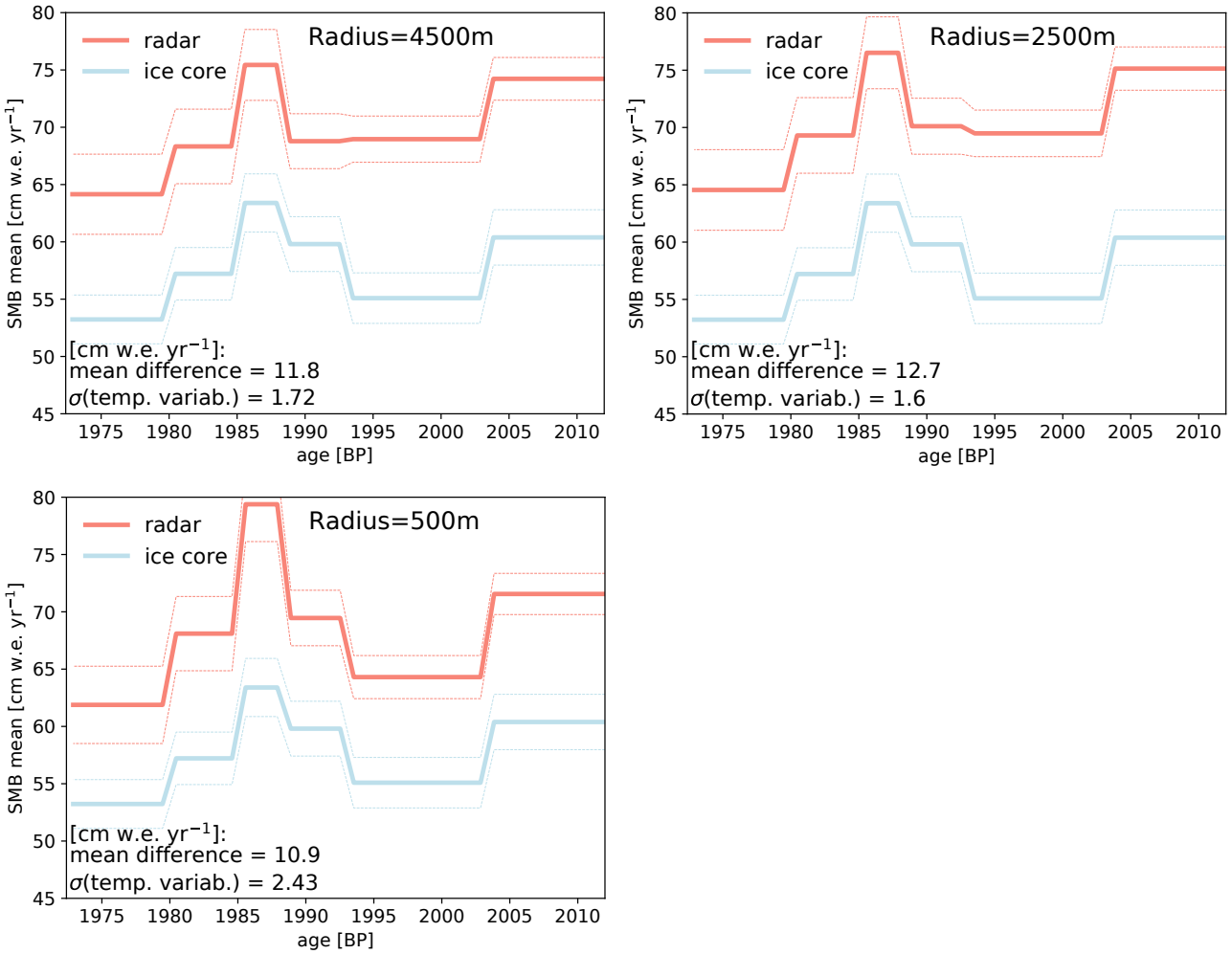


**Fig. S10.** SMB record measured from the ice core (blue line) versus the gridded radar survey mean for decreasing radial distances from the ice core site (red line), for DIR. Each panel indicates the mean state difference and the standard deviation of the temporal variability (given as the difference of the radar and ice core SMB residuals). SMB uncertainty bounds for each record are outlined as dotted lines.

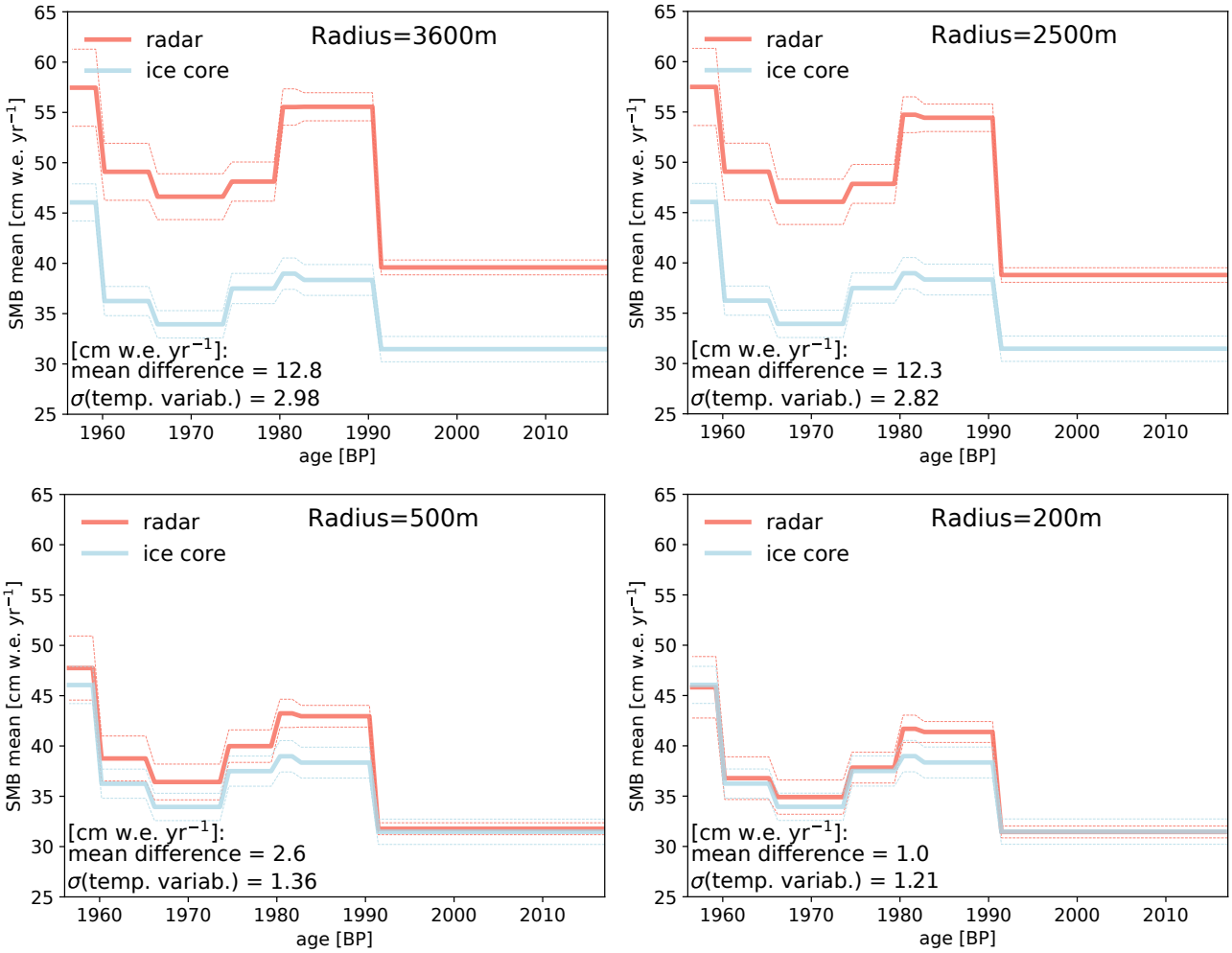


**Fig. S11.** SMB record measured from the ice core (blue line) versus the gridded radar survey mean for decreasing radial distances from the ice core site (red line), for LIR. Each panel indicates the mean state difference and the standard deviation of the temporal variability (given as the difference of the radar and ice core SMB residuals). SMB uncertainty bounds for each record are outlined as dotted lines.

**Table S1.** Ice core-derived SMB for the same time intervals as the IRHs, at each ice rise.

| **IC12** | | **FK17** | | **T18** | |
|---|---|---|---|---|---|
| Time interval | SMB [cm w.e. $yr^{-1}$] | Time interval | SMB [cm w.e. $yr^{-1}$] | Time interval | SMB [cm w.e. $yr^{-1}$] |
| 2012-2003 | 60.4 | 2017-1991 | 31.5 | 2018-2012 | 50.6 |
| 2003-1993 | 55.1 | 1991-1982 | 38.3 | 2012-2008 | 31.1 |
| 1993-1988 | 59.8 | 1982-1980 | 39.0 | 2008-1994 | 32.4 |
| 1988-1985 | 63.4 | 1980-1974 | 37.5 | 1994-1982 | 37.8 |
| 1985-1980 | 57.2 | 1974-1966 | 33.9 | 1982-1971 | 34.4 |
| 1980-1972 | 53.2 | 1966-1960 | 36.3 | 1971-1956 | 33.5 |
| / | / | 1960-1956 | 46.1 | / | / |

largest radial distance away from each ice core site. The survey mean, and standard deviation, of the radar SMB anomaly for each time interval is displayed on each panel. For the ice core (indicated by a colored star), it is simply the SMB measured from which the temporal mean is removed.

## SUPPLEMENT 7: ICE CORE-DERIVED SMB

Table S1 lists the ice core-derived SMB for the same age intervals as for the radar-derived SMB.

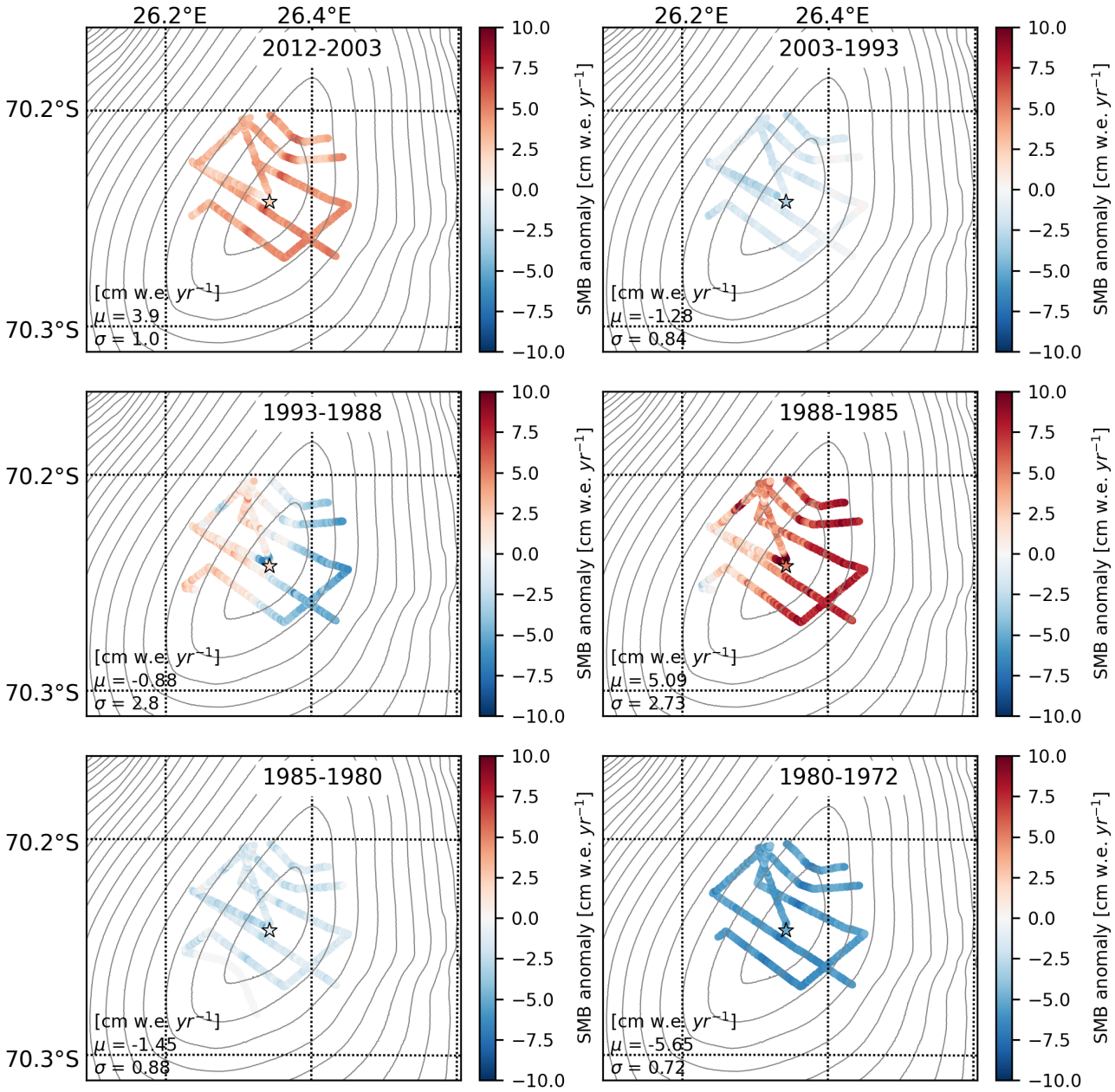


**Fig. S12.** Spatial distribution of the SMB anomalies at DIR. For the ice core (indicated by a colored star), it is simply the SMB measured from which the temporal mean is removed. For the radar survey, we use the 50 × 50 m gridded radar product for a radius of 4 km away from the ice core site. For each grid cell, we calculate the SMB anomaly by subtracting the temporal mean from the calculated SMB record. The spatial mean, and standard deviation, of the radar SMB anomaly for each time interval is displayed on each panel. Contours shown are REMA elevations at 20 m intervals (Howat and others, 2019).

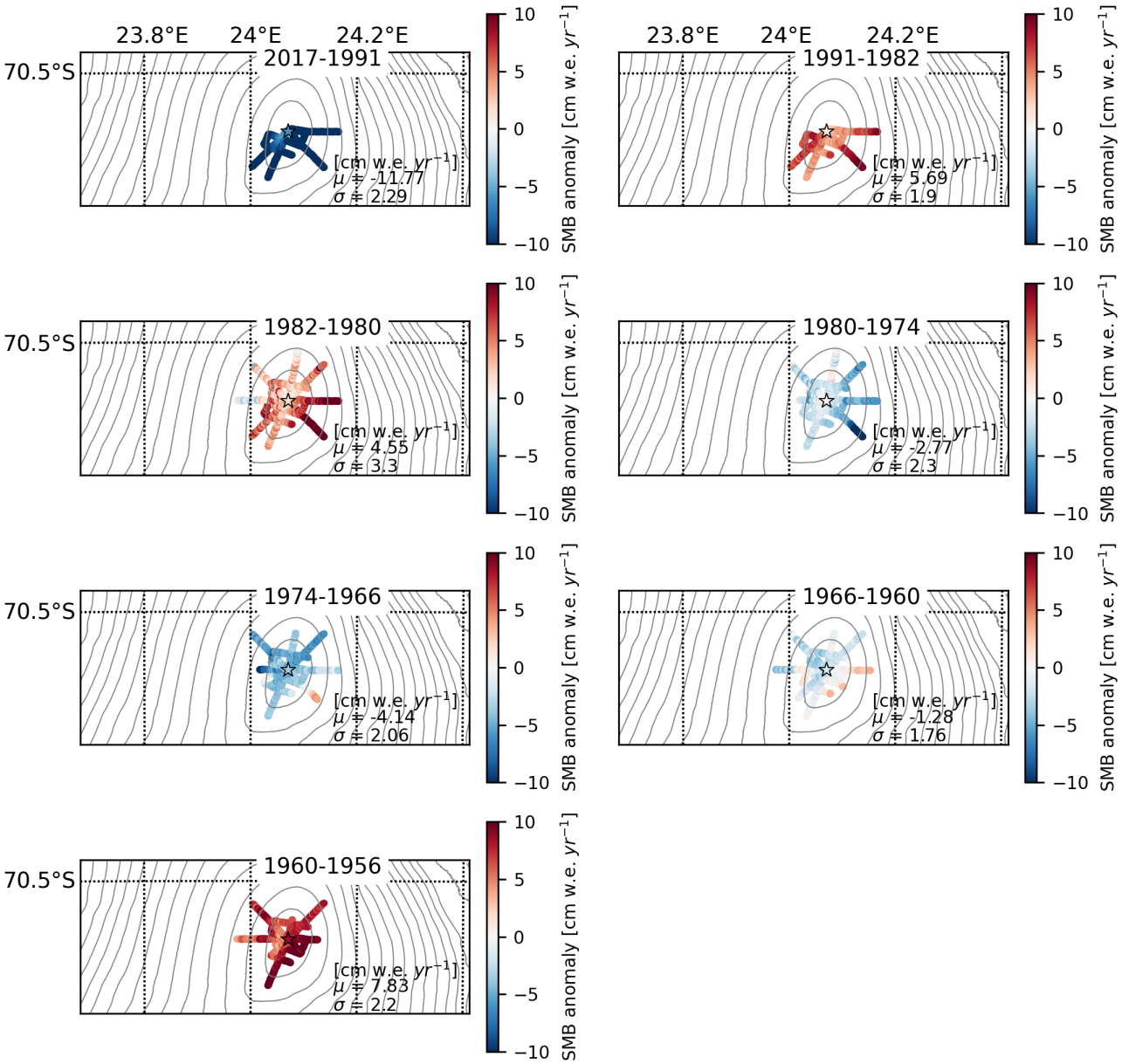


**Fig. S13.** Spatial distribution of the SMB anomalies at LIR. For the ice core (indicated by a colored star), it is simply the SMB measured from which the temporal mean is removed. For the radar survey, we use the 50 × 50 m gridded radar product for a radius of 4 km away from the ice core site. For each grid cell, we calculate the SMB anomaly by subtracting the temporal mean from the calculated SMB record. The spatial mean, and standard deviation, of the radar SMB anomaly for each time interval is displayed on each panel. Contours shown are REMA elevations at 20 m intervals (Howat and others, 2019).

## REFERENCES

Herron MM and Langway CC (1980) Firn densification: An empirical model. *Journal of Glaciology*, **25**(93), 373–385 (doi: 10.3189/S0022143000015239)

Howat IM, Porter C, Smith BE, Noh MJ and Morin P (2019) The Reference Elevation Model of Antarctica. *The Cryosphere*, **13**(2), 665–674 (doi: 10.5194/tc-13-665-2019)

Hubbard B, Tison JL, Philippe M, Heene B, Pattyn F, Malone T and Freitag J (2013) Ice shelf density reconstructed from optical televiewer borehole logging. *Geophysical Research Letters*, **40**(22), 5882–5887 (doi: 10.1002/2013GL058023)

Van Wessem JM, Jan Van De Berg W, Noël BP, Van Meijgaard E, Amory C, Birnbaum G, Jakobs CL, Krüger K, Lenaerts J, Lhermitte S and others (2018) Modelling the climate and surface mass balance of polar ice sheets using RACMO2: Part 2: Antarctica (1979-2016). *The Cryosphere*, **12**(4), 1479–1498